This is the accepted manuscript made available via CHORUS. The article has been published as:

Compressibility of a Fermionic Mott Insulator of Ultracold Atoms

Pedro M. Duarte, Russell A. Hart, Tsung-Lin Yang, Xinxing Liu, Thereza Paiva, Ehsan Khatami, Richard T. Scalettar, Nandini Trivedi, and Randall G. Hulet

Phys. Rev. Lett. **114**, 070403 — Published 20 February 2015

DOI: 10.1103/PhysRevLett.114.070403

Compressibility of a fermionic Mott insulator of ultracold atoms

Pedro M. Duarte,[1] Russell A. Hart,[1] Tsung-Lin Yang,[1] Xinxing Liu,[1] Thereza Paiva,[2]
Ehsan Khatami,[3] Richard T. Scalettar,[4] Nandini Trivedi,[5] and Randall G. Hulet[1,*]

[1]*Department of Physics and Astronomy and Rice Quantum Institute, Rice University, Houston, TX 77005, USA*
[2]*Instituto de Fisica, Universidade Federal do Rio de Janeiro Cx.P. 68.528, 21941-972 Rio de Janeiro RJ, Brazil*
[3]*Department of Physics and Astronomy, San Jose State University, San Jose, CA 95192, USA*
[4]*Department of Physics, University of California, Davis, California 95616, USA*
[5]*Department of Physics, The Ohio State University, Columbus, Ohio 43210, USA*

(Dated: January 23, 2015)

We characterize the Mott insulating regime of a repulsively interacting Fermi gas of ultracold atoms in a three-dimensional optical lattice. We use *in-situ* imaging to extract the central density of the gas, and to determine its local compressibility. For intermediate to strong interactions, we observe the emergence of a plateau in the density as a function of atom number, and a reduction of the compressibility at a density of one atom per site, indicating the formation of a Mott insulator. Comparisons to state-of-the-art numerical simulations of the Hubbard model over a wide range of interactions reveal that the temperature of the gas is of the order of, or below, the tunneling energy scale. Our results hold great promise for the exploration of many-body phenomena with ultracold atoms, where the local compressibility can be a useful tool to detect signatures of different phases or phase boundaries at specific values of the filling.

PACS numbers: 03.75.Ss, 67.85. -d,71.10.Fd

The Hubbard model, which describes spin-1/2 fermions in a lattice with on-site interactions, is one of the fundamental models in quantum many-body physics. It is a notable example of how strongly correlated phases emerge from simple Hamiltonians: it exhibits a Mott insulating regime, antiferromagnetism, and is widely believed to support a d-wave superfluid state in two dimensions (2D), which could explain high-temperature superconductivity as observed in the cuprates [1]. Despite intense efforts, an exact solution of the Hubbard model in more than one dimension and for arbitrary filling has evaded theoretical and computational approaches to this day. Complementing these approaches, the last decade has seen the development of ultracold atoms in optical lattices as a new and versatile platform for the study of many-body physics [2, 3]. In this work, we study a two-spin component degenerate gas of fermions in a simple cubic lattice, a system which realizes the three-dimensional (3D) single band Hubbard model.

Previous ground-breaking experiments investigated the Mott transition in trapped lattice fermions by measuring the variation of the bulk double occupancy with atom number [4–6] and the response of the cloud radius to changes in external confinement [7], both of which are related to the global compressibility. Several key issues, however, remain to be addressed: (i) As bulk measurements are the result of an average over both metallic and insulating phases simultaneously present in the trap, how does the *local* compressibility behave within the trap? (ii) How does the compressibility respond at lower temperatures, as one approaches the magnetic transition? (iii) Can more robust theoretical treatments be employed to benchmark the observed behavior?

In this paper, we address these issues, making significant progress towards understanding the physics of the fermionic Hubbard Hamiltonian through optical lattice emulation. We extract the local compressibility of the gas from a measurement of the *in-situ* density profile, a procedure that has been previously demonstrated for a Fermi gas in a harmonic potential [8], and for lattice bosons [9]. The local compressibility, as well as the central density of the gas, are readily compared with numerical simulations within the local density approximation (LDA). Previous work has shown that the LDA agrees well with numerical calculations of the inhomogeneous Hubbard Hamiltonian away from the quantum critical regime close to the Néel transition [10–12]. The local character of our measurements allows differentiation between the incompressible Mott insulating core and the compressible surrounding metal, thus enabling a more precise characterization of the Mott transition, even at intermediate values of the coupling strength, where magnetic correlations are predicted to be strongest [13–15].

The Hubbard Hamiltonian is given by

$$\hat{H} = -t \sum_{\langle ij \rangle, \sigma} \left(\hat{c}^{\dagger}_{i\sigma} \hat{c}_{j\sigma} + \text{h.c.} \right) + U \sum_{i} \hat{n}_{i\uparrow} \hat{n}_{i\downarrow} - \mu \sum_{i,\sigma} \hat{n}_{i\sigma}. \tag{1}$$

Here, the indices i, j denote lattice sites, the spin states are labeled as $\sigma = \uparrow$ or $\downarrow$, the angled brackets indicate summation over nearest-neighbors, t is the nearest-neighbor tunneling matrix element, U (> 0) is the on-site interaction energy, μ is the chemical potential, $\hat{c}^{\dagger}_{i\sigma}$ ($\hat{c}_{i\sigma}$) is the creation (annihilation) operator for a fermion with spin σ at site i, and $\hat{n}_{i\sigma} = \hat{c}^{\dagger}_{i\sigma} \hat{c}_{i\sigma}$ is the density operator.

For $\mu = U/2$, the average density of the system is $n = 1$ particle per lattice site (half-filling). At half-filling, as the temperature T is reduced, or as U is increased, such that

$T \ll U$, the system undergoes a smooth crossover to a Mott insulating regime, characterized by a suppression of the number of doubly occupied sites and a suppression of density fluctuations, which implies a reduction of the compressibility [16]. If T is reduced below the Néel temperature T_N ($\sim 4t^2/U$ for $U \gg t$), the system undergoes a phase transition to an antiferromagnetic (AFM) state.

Cooling and thermometry have been the greatest challenges for realizing the Hubbard model with ultracold atoms in optical lattices [17]. Even though the temperatures required for pairing and superfluidity in the doped Hubbard model [18] have not yet been reached, the past few years have seen steady experimental progress. This includes the observation of Fermi surfaces in a band insulator [19], the observation of the Mott insulating regime for strong couplings ($U/t \geq 18$) [4, 6, 7] and, more recently, the detection of AFM spin correlations in 1D chains [20, 21] and in a 3D lattice [22].

A vanishing local compressibility characterizes the Mott regime in the Hubbard model. It can also be a useful observable to characterize other phases and models realized with ultracold atoms. For example, kinks in the local compressibility can indicate phase boundaries in the trapped system [23]. The isothermal compressibility of a gas is defined as

$$\kappa = \frac{1}{n^2}\frac{\partial n}{\partial \mu}. \qquad (2)$$

For atoms in a 3D lattice we consider the unitless quantity $(t/a^3)\kappa$, where a is the lattice spacing. In the limit of zero lattice depth, $t \to -\frac{a}{2\pi}\int_{-\pi/a}^{\pi/a}\frac{\hbar^2 q^2}{2m}\exp[iqa]\,\mathrm{d}q = (2/\pi^2)E_r$, where q is the quasimomentum, $E_r = \frac{\hbar^2\pi^2}{2ma^2}$ is the recoil energy, and m is the mass of the particles. For a free Fermi gas with no interactions, the compressibility at zero temperature is given by $\kappa_0 = \frac{3}{2nE_F}$, where E_F is the Fermi energy for each spin component. In this paper we consider the normalized compressibility $\tilde{\kappa}$, defined as

$$\tilde{\kappa} \equiv \frac{(t/a^3)\kappa}{((2\pi^2/E_r)/a^3)\kappa_0} = \frac{(3\pi^2)^{2/3}}{2}\frac{\partial \tilde{n}^{2/3}}{\partial(\mu/t)}, \qquad (3)$$

where $\tilde{n} = a^3 n$.

We start by presenting theoretical results for $\tilde{\kappa}$, which underlie the interpretation of our experimental results. In Fig. 1 we show theoretical results for $\tilde{\kappa}$ at various values of T/t and U/t, obtained using determinantal quantum Monte Carlo (DQMC) [24, 25] and a numerical linked-cluster expansion (NLCE) [26–28] up to the eighth order in the site expansion. These two methods complement each other, and provide results over a wide range of interactions and temperatures. While NLCE can reach lower temperatures than DQMC at large U/t, the opposite is true at weak coupling. Figure 1 shows that the theoretical compressibility diminishes at half-filling and larger U/t as the system enters the Mott insulating regime, and at $\tilde{n} = 2$, where a band insulator forms.

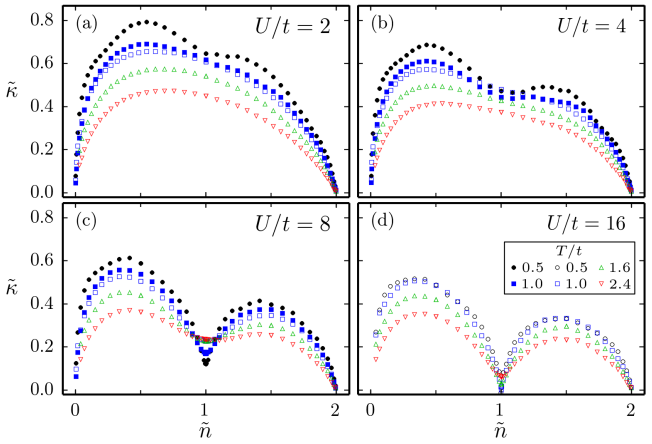

FIG. 1. (color online) Normalized compressibility versus density for the homogeneous 3D Hubbard model, shown for various interaction strengths and temperatures. The different curves were obtained using DQMC (closed symbols) and NLCE (open symbols). At half-filling, $\tilde{n} = 1$, the compressibility vanishes for strong interactions and low temperatures as the system enters the Mott insulating regime.

In addition, Fig. 1 demonstrates that at a temperature $T \leq t$, locally resolving the compressibility enables one to observe the Mott regime for coupling strengths as low as $U/t \sim 8$, in the vicinity of the interaction strength that maximizes T_N [13–15], rather than requiring larger couplings [4, 6, 7].

In our experiment, we produce a two-spin component degenerate Fermi gas of ^{6}Li atoms in the $|F = 1/2; m_F = +1/2\rangle$ and $|F = 1/2; m_F = -1/2\rangle$ hyperfine states, which we label $|\uparrow\rangle$ and $|\downarrow\rangle$, respectively. The apparatus has been described previously [22, 29]. Briefly, the spin mixture is evaporated into a harmonic dimple trap and then loaded into a simple cubic optical lattice. We control the total number of atoms, N, by adjusting the final depth of the dimple trap. The temperature of the atoms in the dimple is measured by fitting the density distribution after time of flight. We obtain $T/T_F = 0.04 \pm 0.02$, independent of N within the range of atom numbers considered for this paper.

The optical lattice is formed by three retroreflected red-detuned (1064 nm) Gaussian laser beams of depth $V_0 = 7\,E_r$. The lattice depth is calibrated via lattice phase modulation spectroscopy, up to a systematic uncertainty of ±5%. Due to the Gaussian beam profiles, the lattice depth decreases with distance from the center, which results in increasing t and decreasing U/t. The lattice depth varies along the 111 body diagonals as $V(r) = V_0\exp[-4r^2/(3w_L^2)]$, where V_0 is the lattice depth at the center, r is the distance from the center, and w_L is the waist ($1/e^2$ radius) of the lattice beams. We make use of the broad Feshbach resonance in ^{6}Li at 832 G [30, 31] to set the on-site interaction strength, U.

The lattice confinement is compensated by the addi-

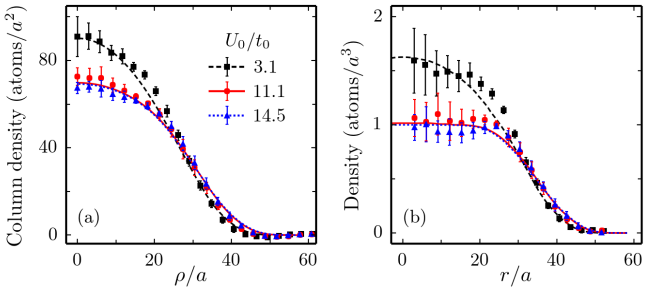

FIG. 2. (color online) (a) Azimuthally averaged column density (including both spin states) vs. distance from the imaging axis ρ, for different values of U_0/t_0. Data points represent the average of eight individual realizations, with error bars corresponding to the standard deviation. The lines in (a) are obtained by integrating the density (calculated for $N = 2\times10^5$ atoms at $T/t_0 = 0.6$) along the imaging axis. (b) Data points correspond to density profiles extracted from the column densities using the inverse Abel transform, where r is the distance from the center of the trap. The lines in (b) show the density calculated for our trap along a body diagonal of the lattice.

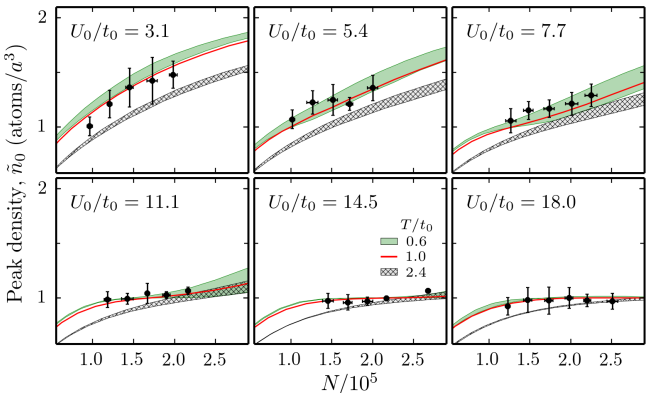

FIG. 3. (color online) Central density, $\tilde{n}_0$ vs. atom number for various interaction strengths. The symbols show the average for a set of 5 to 10 independent realizations, with error bars indicating the standard deviation. The shaded regions are the results of numerical calculations for our trap at $T/t_0 = 0.6$ (solid, green) and 2.4 (crosshatched, gray), with the width of each region corresponding to a ±14% systematic uncertainty in the value of U_0/t_0, arising from the ±5% uncertainty in V_0. The red line is calculated at $T/t_0 = 1.0$, without considering the trap systematics. The calculated density becomes relatively insensitive to uncertainties in U_0/t_0 for the two larger values of U_0/t_0, which are deep in the Mott regime. For $T/t_0 = 0.6$ the total entropy per particle, $S/(Nk_B)$, is between 0.5 and 1.0 for the ranges of N and U_0/t_0 shown in the figure. A temperature of $T/t_0 = 2.4$ is chosen for comparison, as in this case $S/(Nk_B)$ is between 1.5 and 2.4, which is similar to the range between 1.6 and 2.2 reported from the analysis of a previous experiment [37].

tion of three blue-detuned (532 nm) Gaussian beams, which overlap each of the lattice beams but are not themselves retroreflected [22, 32]. The overall confinement in the lattice, which sets the density of the cloud, is adjusted by changing the intensity of the compensation beams. We create samples which appear spherically symmetric with slight adjustment of the intensity of the three independent compensation beams. The average value of the compensation depth is set at $3.8\,E_r$, with a systematic ±10% relative error resulting from the calibration of w_L and the compensation beam waists, w_C. The beam waists along each axis are calibrated by measuring the frequency of radial breathing mode oscillations [28]. We find, up to a ±5% systematic uncertainty, the lattice beam waists to be $w_L = (47; 47; 44)$ µm and the compensation beam waists to be $w_C = (42; 41; 40)$ µm.

We measure the *in-situ* column density distribution of the atoms using polarization phase-contrast imaging [34]. This technique can be used to image dense clouds, in contrast to absorption imaging which is limited to small optical densities due to saturation. The imaging light was detuned by -150 MHz from state $|\uparrow\rangle$ (-74 MHz from $|\downarrow\rangle$), keeping the phase shift across the cloud below $\pi/5$ to avoid significant dispersive distortions of the image.

Figure 2 shows azimuthal averages of the column density and density profiles; the latter are obtained from the former using the inverse Abel transform (which assumes spherical symmetry) [35, 36]. Profiles for three different values of U_0/t_0 (where U_0 and t_0 denote the values of the Hubbard parameters at the center of the trap) are shown, along with profiles calculated for our trap potential.

For the numerical calculations, we set T and the global chemical potential, μ_0, while the local values of U/t, T/t, and μ/t are calculated using the known trap potential. Local values of the density are obtained, within the LDA, by interpolation of NLCE and DQMC results for a homogeneous system calculated in a $(U/t, T/t, \mu/t)$ grid. Because T/t diminishes with r, the lowest value of T/t_0 that can be calculated for the trap is limited to $T/t_0 = 0.6$.

The response of the central density of the cloud, $\tilde{n}_0$, to changes in atom number, is a measure of the local compressibility at the center of the trap. We obtain $\tilde{n}_0$ by fitting the measured column density with the integral, $\int \tilde{n}(\rho, z)\,\mathrm{d}z$, of a flat-topped Gaussian function

$$\tilde{n}(\rho,z) = \begin{cases} \tilde{n}_0 & \text{if} \quad \rho^2 + z^2 < r_0^2 \\ \tilde{n}_0 \exp\left[\frac{r_0^2-\rho^2-z^2}{\sigma^2}\right] & \text{otherwise} \end{cases}, \qquad (4)$$

where ρ is the distance from the imaging axis, and the fit parameters are $\tilde{n}_0$, the flat-top radius, r_0, and the Gaussian $1/e$ radius of the cloud's wings, σ. In Fig. 3 we show $\tilde{n}_0$ vs. N for various values of the interaction strength U_0/t_0. The appearance of a plateau in $\tilde{n}_0$ around 1 is characteristic of the Mott insulating regime. The persistence of a Mott plateau at intermediate coupling, $U_0/t_0 = 11.1$, indicates that the temperature is at or below the tunneling energy, as shown by comparison with

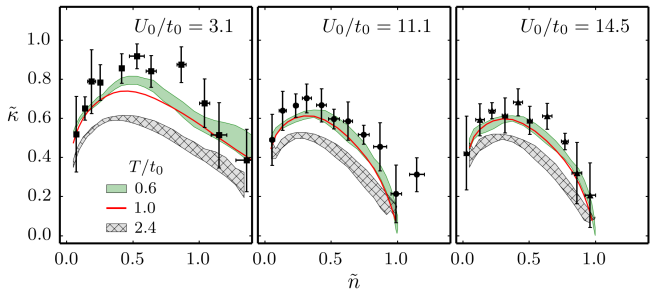

FIG. 4. (color online) Normalized local compressibility, $\tilde{\kappa}$ versus density for different values of U_0/t_0. Closed symbols show the average of eight individual realizations with error bars indicating the standard deviation. The shaded regions are numerical calculations at $T/t_0 = 0.6$ (solid, green) and $T/t_0 = 2.4$ (crosshatched, gray) for $N = 2 \times 10^5$, where the width of the region reflects a $\pm 14\%$ systematic uncertainty in U_0/t_0. The red line is calculated at $T/t_0 = 1.0$, without considering the trap systematics. With $N = 2 \times 10^5$, the total entropy per particle at $T/t_0 = 0.6$ is approximately $S/(Nk_B) = 0.58$, 0.76, and 0.82 for $U_0/t_0 = 3.1$, 11.1, and 14.5, respectively; at $T/t_0 = 2.4$ it is approximately $S/(Nk_B) = 1.59$, 1.70, and 1.66, respectively.

the numerical results. A precise temperature determination is prevented by the fact that the density and other observables related to the charge degrees of freedom, are relatively insensitive to temperature for $T < t$.

The local compressibility, $\tilde{\kappa}$, is obtained by taking a derivative of the measured and calculated density profiles as

$$\tilde{\kappa} = \frac{(3\pi^2)^{2/3}}{2} \frac{\partial \tilde{n}^{2/3}}{\partial r} \left(\frac{\partial(\mu/t)}{\partial r} \right)^{-1}, \qquad (5)$$

where the spatial derivative of the local chemical potential depends only on the trap parameters. For the data, the azimuthal average of the column density, and the inverse Abel transform are noisy at small radii, so, to avoid excessive noise in the determination of the radial derivative of $\tilde{n}^{2/3}$, we restrict our analysis to $r/a > 12$. Figure 4 shows $\tilde{\kappa}$ vs $\tilde{n}$ for the experimental data and for density profiles calculated at different temperatures. A decrease of the compressibility near $\tilde{n} \approx 1$, as expected for a Mott insulator, is observed for $U_0/t_0 = 11.1$ and 14.5. As with the central density, the weak sensitivity of $\tilde{\kappa}$ to T at lower temperatures prevents us from making a precise temperature measurement. However, the comparison of the data with the numerical calculations at $T/t_0 = 0.6$, in both Figs. 3 and 4, reveals that the results are consistent with our previous measurement in the same system, where using spin-sensitive Bragg scattering of light, we determined the temperature to be $T/t_0 = 0.58 \pm 0.07$ [22, 38, 39].

We have shown that the local compressibility of a two-component Fermi gas in an optical lattice may be extracted from *in-situ* measurements of the column density. The data presented here shows evidence of Mott-insulating behavior for interaction strengths as low as $U_0/t_0 = 11$, close to where T_N is expected to be maximal, and where AFM correlations were observed to be maximal for this system [22]. A key achievement of this work is the combination of experiment with two complimentary theoretical approaches which span the full range of U/t and $\tilde{n}$ required to model the trapped atom data. As described in the supplemental material [33], the use of DQMC and NLCE in tandem provides reliable results over a range of temperatures and interaction strengths beyond those available previously.

Measurements of local compressibility in an optical lattice, along with recently developed methods for detecting magnetic order, can improve our understanding of the onset of Mott insulating behavior in the Hubbard model, and answer open questions about its proximity to the AFM phase in different coupling regimes. In addition, the local compressibility can have important implications for understanding the nature and extent of the non-Fermi liquid state of the 2D Hubbard model away from half-filling [44–46] at relatively high temperatures [47]. Finally, as has been recently shown [48, 49], sharp signatures of phase separation and stripe formation are evident in the compressibility, raising the possibility that this central property of cuprate superconductors, and of the Hubbard model, might be accessible to this diagnostic.

This work was supported under ARO Grant No. W911NF-13-1-0018 with funds from the DARPA OLE program, NSF, ONR, the Welch Foundation (Grant No. C-1133), and ARO-MURI Grant No. W911NF-14-1-0003. T.P. acknowledges support from CNPq, FAPERJ, and the INCT on Quantum Information. N.T. acknowledges support from grant No. NSF-DMR1309461. R.T.S. acknowledges support from the University of California, Office of the President. T.P. and R.T.S. acknowledge funding from Science Without Borders, Brazil.

* randy@rice.edu

[1] P. W. Anderson, Science **235**, 1196 (1987).
[2] I. Bloch, J. Dalibard, and W. Zwerger, Rev. Mod. Phys. **80**, 885 (2008).
[3] D. Jaksch and P. Zoller, Ann. Phys. **315**, 52 (2005).
[4] R. Jördens, N. Strohmaier, K. Günter, H. Moritz, and T. Esslinger, Nature **455**, 204 (2008).
[5] V. W. Scarola, L. Pollet, J. Oitmaa, and M. Troyer, Phys. Rev. Lett. **102**, 135302 (2009).
[6] S. Taie, R. Yamazaki, S. Sugawa, and Y. Takahashi, Nat. Phys. **8**, 825 (2012).
[7] U. Schneider, L. Hackermüller, S. Will, T. Best, I. Bloch, T. A. Costi, R. W. Helmes, D. Rasch, and A. Rosch, Science **322**, 1520 (2008).
[8] Y.-R. Lee, M.-S. Heo, J.-H. Choi, T. T. Wang, C. A. Christensen, T. M. Rvachov, and W. Ketterle, Phys. Rev. A **85**, 063615 (2012).

[9] N. Gemelke, X. Zhang, C.-L. Hung, and C. Chin, Nature **460**, 995 (2009).

[10] M. Rigol, A. Muramatsu, G. G. Batrouni, and R. T. Scalettar, Phys. Rev. Lett. **91**, 130403 (2003).

[11] R. W. Helmes, T. A. Costi, and A. Rosch, Phys. Rev. Lett. **100**, 056403 (2008).

[12] S. Chiesa, C. N. Varney, M. Rigol, and R. T. Scalettar, Phys. Rev. Lett. **106**, 035301 (2011).

[13] R. Staudt, M. Dzierzawa, and A. Muramatsu, The European Physical Journal B - Condensed Matter and Complex Systems **17**, 411 (2000).

[14] T. Paiva, Y. L. Loh, M. Randeria, R. T. Scalettar, and N. Trivedi, Phys. Rev. Lett. **107**, 086401 (2011).

[15] E. Kozik, E. Burovski, V. W. Scarola, and M. Troyer, Phys. Rev. B **87**, 205102 (2013).

[16] L. De Leo, C. Kollath, A. Georges, M. Ferrero, and O. Parcollet, Phys. Rev. Lett. **101**, 210403 (2008).

[17] D. C. McKay and B. DeMarco, Rep. Prog. Phys. **74**, 054401 (2011).

[18] W. Hofstetter, J. I. Cirac, P. Zoller, E. Demler, and M. D. Lukin, Phys. Rev. Lett. **89**, 220407 (2002).

[19] M. Köhl, H. Moritz, T. Stöferle, K. Günter, and T. Esslinger, Phys. Rev. Lett. **94**, 080403 (2005).

[20] D. Greif, T. Uehlinger, G. Jotzu, L. Tarruell, and T. Esslinger, Science **340**, 1307 (2013).

[21] J. Imriška, M. Iazzi, L. Wang, E. Gull, D. Greif, T. Uehlinger, G. Jotzu, L. Tarruell, T. Esslinger, and M. Troyer, Phys. Rev. Lett. **112**, 115301 (2014).

[22] R. A. Hart, P. M. Duarte, T.-L. Yang, X. Liu, T. Paiva, E. Khatami, R. T. Scalettar, N. Trivedi, D. A. Huse, and R. G. Hulet, arXiv:1407.5932v1 [cond-mat.quant-gas].

[23] Q. Zhou, Y. Kato, N. Kawashima, and N. Trivedi, Phys. Rev. Lett. **103**, 085701 (2009).

[24] R. Blankenbecler, D. J. Scalapino, and R. L. Sugar, Phys. Rev. D **24**, 2278 (1981).

[25] T. Paiva, R. Scalettar, M. Randeria, and N. Trivedi, Phys. Rev. Lett. **104**, 066406 (2010).

[26] M. Rigol, T. Bryant, and R. R. P. Singh, Phys. Rev. Lett. **97**, 187202 (2006).

[27] E. Khatami and M. Rigol, Phys. Rev. A **84**, 053611 (2011).

[28] See Methods in Ref. [11] for more details of the expansion used here.

[29] P. M. Duarte, R. A. Hart, J. M. Hitchcock, T. A. Corcovilos, T.-L. Yang, A. Reed, and R. G. Hulet, Phys. Rev. A **84**, 061406 (2011).

[30] M. Houbiers, H. T. C. Stoof, W. I. McAlexander, and R. G. Hulet, Phys. Rev. A **57**, R1497 (1998).

[31] G. Zürn, T. Lompe, A. N. Wenz, S. Jochim, P. S. Julienne, and J. M. Hutson, Phys. Rev. Lett. **110**, 135301 (2013).

[32] C. J. M. Mathy, D. A. Huse, and R. G. Hulet, Phys. Rev. A **86**, 023606 (2012).

[33] These measurements are performed with sufficiently weak compensation that the potential remains approximately harmonic.

[34] C. C. Bradley, C. A. Sackett, and R. G. Hulet, Phys. Rev. Lett. **78**, 985 (1997).

[35] S. van der Walt, J. L. Schönberger, J. Nunez-Iglesias, F. Boulogne, J. D. Warner, N. Yager, E. Gouillart, T. Yu, and the scikit-image contributors, PeerJ **2**, e453 (2014).

[36] We perform the inverse Abel transform with the filtered back-projection algorithm, as implemented in the scikit-image image processing library [35].

[37] R. Jördens, L. Tarruell, D. Greif, T. Uehlinger, N. Strohmaier, H. Moritz, T. Esslinger, L. De Leo, C. Kollath, A. Georges, V. Scarola, L. Pollet, E. Burovski, E. Kozik, and M. Troyer, Phys. Rev. Lett. **104**, 180401 (2010).

[38] T. A. Corcovilos, S. K. Baur, J. M. Hitchcock, E. J. Mueller, and R. G. Hulet, Phys. Rev. A **81**, 013415 (2010).

[39] Note that in Ref. [22] the value of T/t was quoted using the value of t at the radius where AFM spin correlations are maximal, instead of t_0 as used here.

[40] See Supplemental Material [url], which includes Refs.[41–43], for a comparison of various theoretical methods.

[41] S. Fuchs, E. Gull, L. Pollet, E. Burovski, E. Kozik, T. Pruschke, and M. Troyer, Phys. Rev. Lett. **106**, 030401 (2011).

[42] G. Rohringer, A. Toschi, A. Katanin, and K. Held, Phys. Rev. Lett. **107**, 256402 (2011).

[43] J. Henderson, J. Oitmaa, and M. Ashley, Phys. Rev. B **46**, 6328 (1992).

[44] C. M. Varma, P. B. Littlewood, S. Schmitt-Rink, E. Abrahams, and A. E. Ruckenstein, Phys. Rev. Lett. **63**, 1996 (1989).

[45] N. S. Vidhyadhiraja, A. Macridin, C. Şen, M. Jarrell, and M. Ma, Phys. Rev. Lett. **102**, 206407 (2009).

[46] G. Sordi, P. Sémon, K. Haule, and A.-M. Tremblay, Sci. Rep. **2** (2012).

[47] K. Mikelsons, E. Khatami, D. Galanakis, A. Macridin, J. Moreno, and M. Jarrell, Phys. Rev. B **80**, 140505 (2009).

[48] E. Khatami, K. Mikelsons, D. Galanakis, A. Macridin, J. Moreno, R. T. Scalettar, and M. Jarrell, Phys. Rev. B **81**, 201101 (2010).

[49] E. Gull, O. Parcollet, P. Werner, and A. J. Millis, Phys. Rev. B **80**, 245102 (2009).